metals

MDPI

Article

Exothermic and Slag Formation Behavior of Aluminothermic Reduction of Mo and V Oxides

Xiaoshu Wang [1], Jinfa Liao [1,2,*], Xiaodong Ma [3] and Baojun Zhao [1,2]

[1] School of Metallurgical Engineering, Jiangxi University of Science and Technology, Ganzhou 341000, China; bzhao@jxust.edu.cn (B.Z.)
[2] National Innovation Center for Rare Earth Functional Materials, Ganzhou 341000, China
[3] Sustainable Minerals Institute, The University of Queensland, Brisbane, QLD 4072, Australia; x.ma@uq.edu.au
* Correspondence: liaojinfa@jxust.edu.cn

Abstract

Vanadium (V), molybdenum (Mo), and aluminum (Al) are important alloying elements in titanium alloys, typically introduced through master alloys such as V-Al and Mo-Al. Current preparation of these master alloys predominantly relies on the spontaneous reduction of V_2O_5 or MoO_3 by aluminum. However, separate production and addition of master alloys increase the cost of the titanium alloy. Insufficient understanding of the exothermic behavior and slag-forming process during the aluminothermic reaction often leads to low alloy yield and elevated impurity levels due to splashing and poor alloy–slag separation. This study focused on the controllable aluminothermic reaction of V_2O_5 and MoO_3 to produce high-quality and high-yield V/Al/Mo alloy. Thermodynamic calculations indicate that the reduction of MoO_3 to Mo by aluminum is more favorable than the reduction of V_2O_5 to V. Al% in the V-Al-Mo alloy is crucial for controlling reaction temperature. When the Al/O ratio in the raw materials exceeds 1.0, increasing aluminum reduces both the reaction exothermicity and theoretical reaction temperature. A combination of thermodynamic calculations and high-temperature experiments demonstrates that the heat generation and slag composition can be effectively controlled by Al/O ratio in raw materials. When the Al/O ratio in raw materials is 1.6–2.0, the yields of Mo and V exceed 99% and 95%, respectively. This study provides an effective approach to producing V/Al/Mo alloy under controllable conditions, which shows great potential for other aluminothermic reactions. Extensive solid solutions of V/Al/Mo also provide invaluable data for the optimization of the alloy database.

Keywords: V-Al-Mo alloy; titanium alloy; aluminothermic reaction; V_2O_5; MoO_3

check for updates

Academic Editors: Srecko Stopic and Dmitri Molodov

Received: 25 April 2025
Revised: 10 June 2025
Accepted: 22 June 2025
Published: 25 June 2025

Citation: Wang, X.; Liao, J.; Ma, X.; Zhao, B. Exothermic and Slag Formation Behavior of Aluminothermic Reduction of Mo and V Oxides. *Metals* **2025**, *15*, 704. https://doi.org/10.3390/met15070704

Copyright: © 2025 by the authors. Licensee MDPI, Basel, Switzerland. This article is an open access article distributed under the terms and conditions of the Creative Commons Attribution (CC BY) license (https://creativecommons.org/licenses/by/4.0/).

1. Introduction

Titanium alloys, renowned for their high specific strength, exceptional resistance to extreme temperatures, superior corrosion resistance, excellent weldability, and biocompatibility, have emerged as core materials in aerospace, marine engineering, energy chemical industries, and biomedical applications [1–4]. Their strategic significance is particularly pronounced in aerospace, where the escalating demand for lightweight materials capable of withstanding extreme operational conditions has solidified their indispensable role [5–8]. The performance of titanium alloys is intrinsically linked to the selection and precise proportioning of alloying elements. Aluminum (Al), functioning as an α-phase stabilizer, enhances both ambient and high-temperature mechanical properties via solid

solution strengthening, while molybdenum (Mo) and vanadium (V), acting as isomorphous β-phase stabilizers, optimize heat treatment responsiveness and improve strength toughness synergy [9–13]. Currently, Al, Mo, and V are predominantly introduced into titanium melt as binary master alloys (e.g., Al-Mo and Al-V). However, the production of the master alloys separately increases their cost. The sequential addition of multiple components complicates the smelting process and exacerbates compositional segregation [14]. Development of V/Al/Mo multicomponent master alloys presents a viable solution to these challenges.

Preparation of V/Al/Mo alloys primarily relies on the simultaneous aluminothermic reduction of MoO_3 and V_2O_5, a process whose exothermic characteristics critically influence alloy yield and purity. Zhang et al. [15] attempted to synthesize V/Al/Mo alloys via ex-furnace aluminothermic methods, but inadequate control over reaction intensity resulted in heterogeneous microstructures and elevated impurity levels. Alternative approaches, such as pre-pelletizing MoO_3 and V_2O_5 powders to mitigate splattering [16], face challenges including silicon contamination from binders and inconsistent pellet size distribution, thereby compromising process stability and product quality.

Suboptimal reaction conditions may induce splashing, raw material loss, low alloy yield, and impurity accumulation, collectively degrading alloy quality and escalating production costs [17–19]. Research has demonstrated that tailored strategies, such as raw material design (e.g., employing low-valent vanadium oxides [20–22]), slag composition modulation (e.g., CaO addition [23,24]), cooling material incorporation [25,26], and electric furnace control [27,28], can balance exothermic behavior and enhance slag-metal separation. For instance, Sun [20] used a V_2O_5 and V_2O_3 mixture to control the heat for vanadium–aluminum alloy production. Similarly, Yee et al. [27] revealed that moderate CaO additions (6–8 wt.%) promoted the formation of low-melting-point slag phases (e.g., $CaO{\cdot}Al_2O_3$), whereas excessive CaO (>12 wt.%) generated refractory phases (e.g., $CaO{\cdot}6Al_2O_3$), impairing slag fluidity. Despite these advancements, critical gaps persist in the aluminothermic reduction of V-Mo oxides: (1) the thermodynamic competition mechanisms governing multi-oxide co-reduction remain unclear; (2) strategies to suppress reaction violence and splashing are underdeveloped; (3) achieving compositional homogeneity and impurity control in the alloys remains challenging.

To address these issues, this study proposes a simultaneous aluminothermic reduction process utilizing V_2O_5, MoO_3, CaO, and Al as raw materials. Through integrated thermodynamic simulations and experimental validation, we elucidate the preferential reduction sequence of MoO_3 versus V_2O_5, establish quantitative correlations between the aluminum-to-oxygen ratio (Al/O) and reaction temperature/phase composition, and optimize process parameters to achieve high-yield (Mo > 99%, V > 95%), low-impurity, and compositionally controlled V/Al/Mo alloys. This work provides both theoretical insights and practical methodologies for advancing the cost-effective production of high-performance titanium alloys.

2. Research Methodology

2.1. Raw Materials and Experimental Plan

The raw materials used in this study include V_2O_5, MoO_3, aluminum granules, and calcium oxide (CaO). Detailed specifications of these materials are summarized in Table 1.

Table 1. Raw materials used in the present work.

Material	Form	Purity (%)	Manufacturer
V_2O_5	Powder	≥99.7	Chengde Vanadium Titanium Co., Ltd. (Chengdu, China)
Al	Granules	≥99.9	Beijing Kerry New Materials Co., Ltd. (Beijing, China)
CaO	Powder	≥99.5	Xilong Scientific Co., Ltd. (Shantou, China)
MoO_3	Powder	≥99.5	Shanghai Macklin Biochemical Co., Ltd. (Shanghai, China)

During the production of V/Al/Mo alloy, excess metallic aluminum reacts with V_2O_5 and MoO_3 through an aluminothermic reduction process. The resultant metallic vanadium (V) and molybdenum (Mo) subsequently combine with excess aluminum to form the V/Al/Mo alloy. The ratio of V to Mo in the alloy was kept at 1:1, which is a typical one in Ti alloys. The concentrations of (V + Mo) are primarily controlled by the excess aluminum used in the reaction system. The principal chemical reactions and physical process reactions are:

(i) Chemical reactions: Reduction of V_2O_5 and MoO_3 by Al (Equation (1)), supported by stoichiometry and exothermicity;

(ii) Physical process: Alloy formation of V, Mo, and excess Al (Equation (2)). This distinction ensures accurate representation of both the redox chemistry and solid-state alloying. The V:Mo = 1:1 ratio and the role of excess Al in controlling (V + Mo) content are retained.

$$12Al + 3V_2O_5 + MoO_3 = 6Al_2O_3 + 6V + Mo \quad (1)$$

$$Al + V + Mo \rightarrow V/Al/Mo\ alloy \quad (2)$$

The aluminum in the reactants serves dual roles as both reducing agent and alloying element. The total aluminum requirement equals the sum of: (1) aluminum consumed in Reaction (1) for oxide reduction and (2) aluminum incorporated into the alloy in Reaction (2). Al/O is used to express the amount of aluminum required to complete Reaction (1) as a reducing agent. The compositions and weights of slags are planned to be the same in all experiments. Detailed experimental conditions are provided in Table 2.

Table 2. Experimental conditions.

Exp No.	Al (g)	V_2O_5 (g)	MoO_3 (g)	CaO (g)	Al:V:Mo in Alloy	Al in Alloy (wt%)	Al/O (wt)
#1	2.8	3.0	2.5	4.5	2:9:9	10	1.2
#2	3.3	3.0	2.5	4.5	1:2:2	20	1.4
#3	3.9	3.0	2.5	4.5	6:7:7	30	1.6
#4	4.7	3.0	2.5	4.5	4:3:3	40	2.0
#5	5.8	3.0	2.5	4.5	2:1:1	50	2.4
#6	7.4	3.0	2.5	4.5	3:1:1	60	3.1

2.2. Experimental Procedure

The powders of V_2O_5, MoO_3, and CaO were dried at 120 °C for 2 h to remove moisture and then mixed in an agate mortar according to the predetermined ratio for 30 min. The mixture was mixed with aluminum particles (~1 mm) evenly and pelletized in a stainless steel mold (inner diameter: 2 cm). The pellets were subsequently loaded into a high-purity alumina crucible (purity ≥ 99%, dimensions: 25 mm inner diameter × 55 mm height), which was nested inside a graphite crucible. The crucible assembly was supported by a

thermocouple sheath and positioned within the isothermal zone of a high-temperature tube furnace. A type-B thermocouple inside an alumina protection sheath was embedded in an upside-down graphite crucible to continuously monitor the temperature during the reaction. A schematic diagram of the experimental setup is shown in Figure 1.

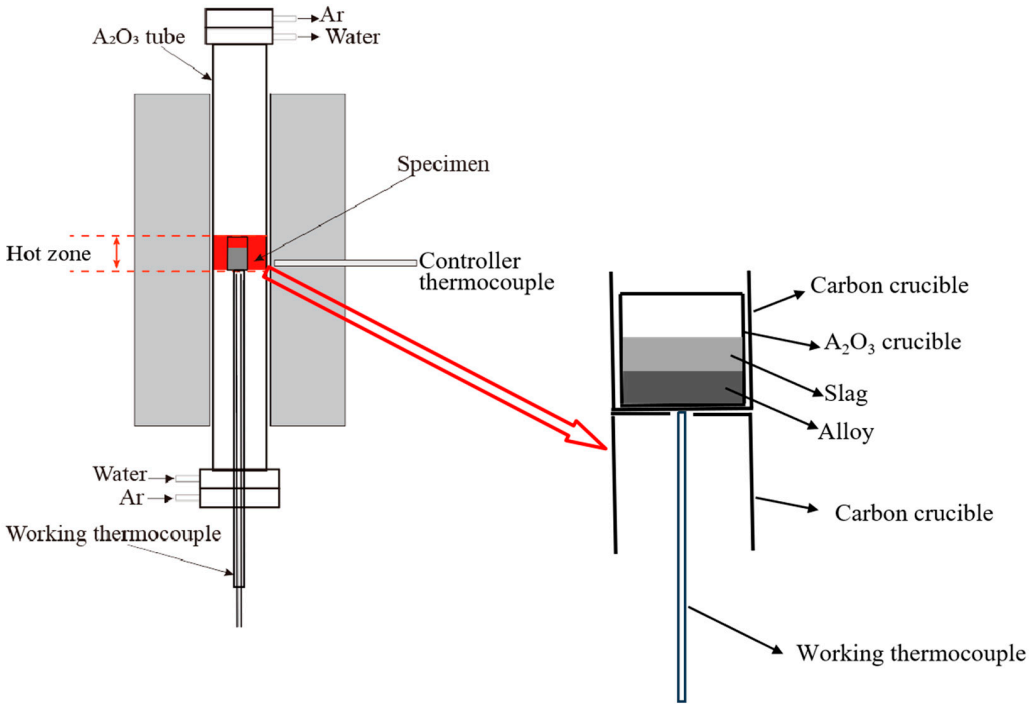


Figure 1. A schematic diagram of the experimental setup.

The entire experiment was conducted under an argon protective atmosphere to prevent oxidation of metallic aluminum and the resulting V/Al/Mo alloy at high temperatures. The sample was precisely positioned in the furnace's hot zone, with real-time temperature monitoring via a high-precision Type B thermocouple for precise thermal control. A programmed heating profile was implemented to optimize alloy quality and slag separation: the temperature was raised at 10 °C/min to 1550 °C, followed by a 15-min hold to achieve thermal equilibrium, promote slag–alloy segregation, and enhance elemental diffusion for the uniform microstructure and composition of the alloy. The experiments were conducted according to the ratios/proportions outlined in Table 2. After the aluminothermic reaction, all samples were cooled to room temperature in the furnace. The crucible was then carefully fractured to retrieve the alloy and slag, which underwent subsequent microstructural analysis and compositional testing to evaluate phase distribution and elemental homogeneity.

2.3. Sample Characterization

Both slag and alloy samples were mounted in epoxy resin and subjected to sequential grinding and polishing. Microstructural features and polishing quality were examined using a LEICA DMC5400 optical microscope (Leica, Wetzlar, Germany, Europe) Phase compositions and microstructure were analyzed with a JXA-ISP100 electron probe microanalyzer (JEOL, Tokyo, Japan). The standards used for EPMA included alumina (Al_2O_3) for Al, magnesia (MgO) for Mg, wollastonite ($CaSiO_3$) for Ca and Si, vanadium for V, and molybdenum for Mo. Note that EPMA can only measure elemental composition. All vanadium oxides in different electronic states are expressed as "V_2O_5" for presentation purposes. Bulk chemical compositions of the alloy and slag were determined using an

Agilent ICPOES730 (Agilent, Santa Clara, CA, USA) inductively coupled plasma optical emission spectrometer (ICP-OES).

2.4. Thermodynamic Predictions

The FactSage 8.3 software [29,30] provides preliminary information for slag design and metallurgical process optimization, reducing the number of high-temperature experiments. In this study, thermodynamic calculations were performed using FactSage 8.3. The Reaction module was employed to calculate the Gibbs free energy of the aluminothermic reactions, while the Equilib module simulated thermodynamic equilibrium conditions. Selected databases included FactPS, FToxid, and SGnobl, with configured solution phases, FToxid-SLAGA, FToxid-SPINC, FToxid-MeO_A, FToxid-CORU, FToxid-VO_ and SpMCBN-LIQU.

3. Thermodynamic Analysis of Aluminothermic Reactions

3.1. Gibbs Free Energy and Enthalpy Changes in Aluminothermic Reactions

In aluminothermic reduction processes, aluminum acts as a reducing agent to progressively reduce vanadium oxides to V. The reactions using different vanadium oxides can be described as follows:

$$Al + 0.3\ V_2O_5 = 0.5\ Al_2O_3 + 0.6\ V \quad (3)$$

$$Al + 0.375\ V_2O_4 = 0.5\ Al_2O_3 + 0.75\ V \quad (4)$$

$$Al + 0.5\ V_2O_3 = 0.5\ Al_2O_3 + V \quad (5)$$

$$Al + 1.5\ VO = 0.5\ Al_2O_3 + 1.5\ V \quad (6)$$

Similarly, the overall aluminothermic reduction reaction for molybdenum oxide can be expressed as:

$$Al + 0.5\ MoO_3 = 0.5\ Al_2O_3 + 0.5\ Mo \quad (7)$$

For the Al-V_2O_5 system, researchers such as Jing et al. [31], Duan et al. [32], and Yin et al. [33] investigated the thermal behavior of aluminothermic reactions using differential scanning calorimetry (DSC) at varying heating rates. Their results revealed an endothermic peak near 660 °C, corresponding to the melting of aluminum, and a minor exothermic peak within 670–700 °C, attributed to the initiation of the aluminothermic reaction, indicating that the reaction commences after aluminum melting. The standard molar Gibbs free energy change for a reaction can be expressed in two conventions: (1) based on the formation of 1 mole of compound; (2) based on the reaction of 1 mole of elemental reactant [34]. In this study, the Reaction module of FactSage was employed to calculate the Gibbs free energy changes (ΔG) and enthalpy changes (ΔH) for Reactions (3)–(7) at 660 °C (aluminum melting point), using the 1-mole elemental reactant (Al) convention. The computational results are illustrated in Figure 2a.

The x-axis in Figure 2a represents the reduction of vanadium oxides from different oxidation states to metallic vanadium, while the y-axis indicates the corresponding Gibbs free energy and enthalpy changes. The reduction of MoO_3 to metallic Mo is also included for comparison. The results in Figure 2a reveal the following:

(1) All reactions exhibit negative values for both Gibbs free energy (ΔG) and enthalpy changes (ΔH), confirming that these reactions are thermodynamically spontaneous and exothermic at 660 °C.

(2) Comparing the free energy and enthalpy changes for the reduction of vanadium oxides from different oxidation states to metallic vanadium, higher oxidation states (e.g., V^{5+} in V_2O_5) demonstrate greater thermodynamic favorability and release more heat. Notably, the reduction of MoO_3 to metallic Mo is thermodynamically more

favorable and releases significantly more heat compared to the reduction of V_2O_5 to metallic V.

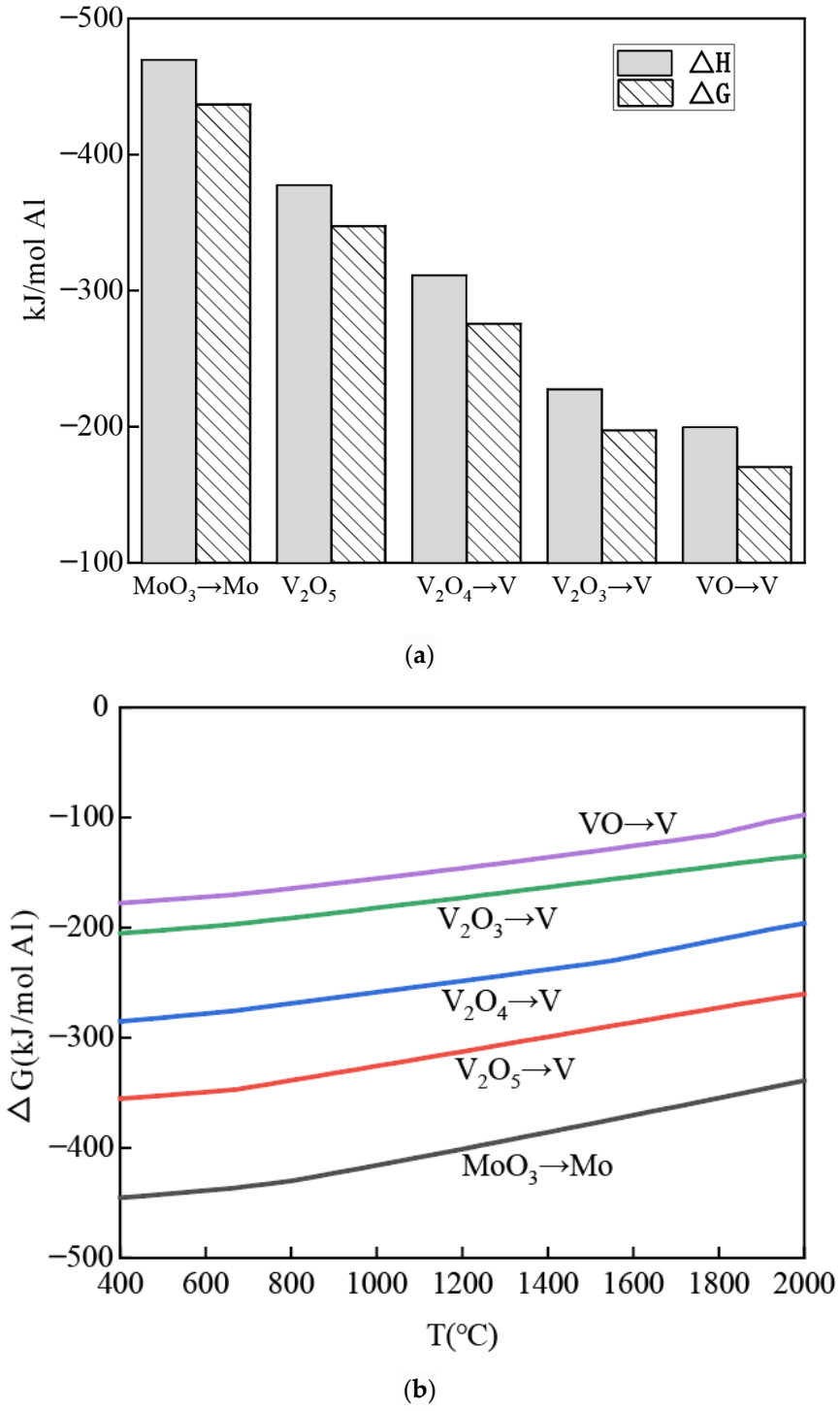


Figure 2. (**a**) Gibbs free energy and enthalpy changes of reactions (3) to (7) at 660 °C; (**b**) Gibbs free energy changes as a function of temperature for reactions (3) to (7).

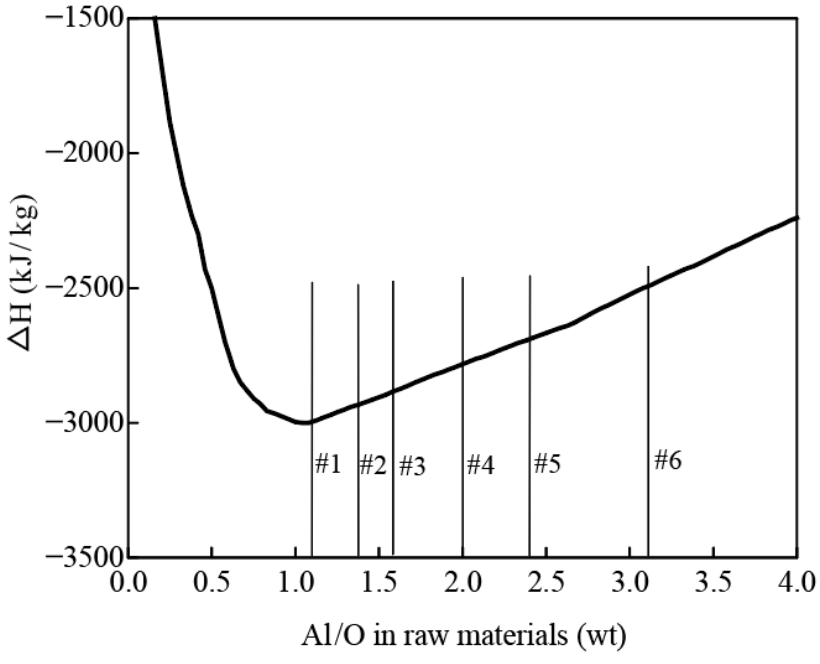
Figure 2b shows the Gibbs free energy changes as a function of temperature for reactions (3) to (7). Because all aluminothermic reactions are exothermic, ΔG of the reactions (3) to (7) increases with increasing temperature. Negative ΔG indicates that all reactions shown in Figure 2b are thermodynamically spontaneous, and the order of the reaction tendency does not change up to 2000 °C.

3.2. Thermodynamic Analysis of the Reaction System

As shown in Figure 2, the aluminothermic reduction reaction releases substantial heat, which elevates the system temperature. Assuming no heat loss, the maximum reaction temperature (T_{max}) can be calculated based on the actual mass of raw materials. The calculation method is as follows: under the experimental conditions listed in Table 2, using V_2O_5, Al, MoO_3, and CaO as starting materials, and assuming complete reduction, the compositions and masses of all slags are fixed as the same, while the mass ratio of V to Mo in the alloy is maintained at 1:1. The Equilib module in FactSage was employed to simulate the reactions shown in Table 2. The FactPS, FToxid, and SGnobl databases were selected for the calculations. The heat released per kg of reactants (unit heat) is presented in Figure 3a as a function of Al/O in raw materials. Assuming the $\Delta H = 0$ and the reaction system is closed, the maximum reaction temperature T_{ma}, as a function of Al/O in raw materials, is shown in Figure 3b.

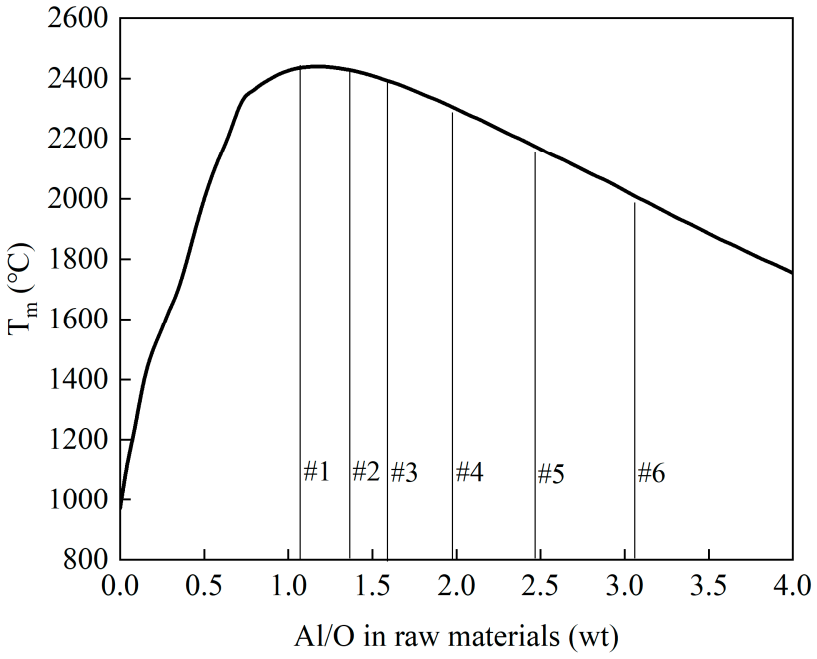
It can be seen from Figure 3 that the aluminum addition significantly influences the unit heat and T_m. When Al/O < 1, unit heat and T_m rise rapidly with increasing Al/O ratios because all aluminum reacts with the oxides as a reducing agent, releasing heat from the reaction and raising the system temperature. At Al/O = 1, the system reaches its theoretical maximum temperature (2442 °C), where the oxides of vanadium and molybdenum are fully reduced. However, when Al/O > 1, excess aluminum only reacts with the V and Mo to form a V/Al/Mo alloy, increasing the alloy mass and absorbing heat for melting, thereby lowering T_m. When the aluminum content in the alloy increases from 10% (#1) to 60% (6), the unit heat reduces from 2980 to 2500 kJ/kg, and T_m decreases from 2427 to 2002 °C.

Figures 2 and 3 collectively demonstrate that the reaction temperature can be controlled through exothermic or endothermic processes. In practice, using lower-valence oxides (e.g., VO or V_2O_3 instead of V_2O_5) reduces the heat generated, while increasing the mass of the alloy or slag enhances heat absorption, effectively lowering the system temperature. This thermodynamic framework provides critical insights for optimizing industrial aluminothermic processes through stoichiometric adjustments and material selection.



(**a**)

Figure 3. *Cont.*



(**b**)

Figure 3. Heat released from the reaction (**a**) and maximum temperature (**b**) as a function of Al/O weight ratio in raw materials calculated by FactSage 8.3.

4. Experimental Results and Discussion

Figure 4 presents macrographs of post-reaction samples from #1 and #3, illustrating the effects of reaction conditions on alloy–slag separation. When the aluminum content in the alloy is low (e.g., #1 and #2, corresponding to Al/O ratios of 1.2 and 1.4, respectively), the reaction releases significant heat, generating a theoretical maximum temperature over 2400 °C. As shown in Figure 4, under these conditions, the alumina crucible fractures during the reaction, causing melt leakage and incomplete aluminothermic reduction. The alloy yield is minimal, and the alumina crucible sticks with the graphite crucible. In contrast, when the aluminum content in the alloy is high (e.g., #3–#6), the reduced exothermicity lowers the theoretical maximum temperature. This prevents crucible failure, allowing the aluminothermic reaction to proceed to completion. Post-reaction samples exhibit clear separation between the alloy and slag, with intact crucible structures. This phenomenon confirms the critical role of Al/O ratio in balancing exothermicity and thermal management. Excessive heat generation at low Al/O ratios exceeds the crucible's thermal tolerance, while controlled heat release at higher Al/O ratios ensures process stability and product integrity.

As shown in Figure 1, a B-type thermocouple was placed underneath the reaction system to monitor the temperature changes during the reaction. The thermocouple could not measure the real temperature of the sample because it was separated by the alumina sheath, graphite crucible, and alumina crucible. However, the rapidly increased temperature due to the reaction heat can still be observed, as shown in Figure 5. The temperature started to increase between 1477 and 1488 °C, indicating a large amount of heat was generated in this temperature range. The temperature was increased by 39 °C for #3 and 23 °C for #6, respectively, which is consistent with the calculated heat generation shown in Figure 3.

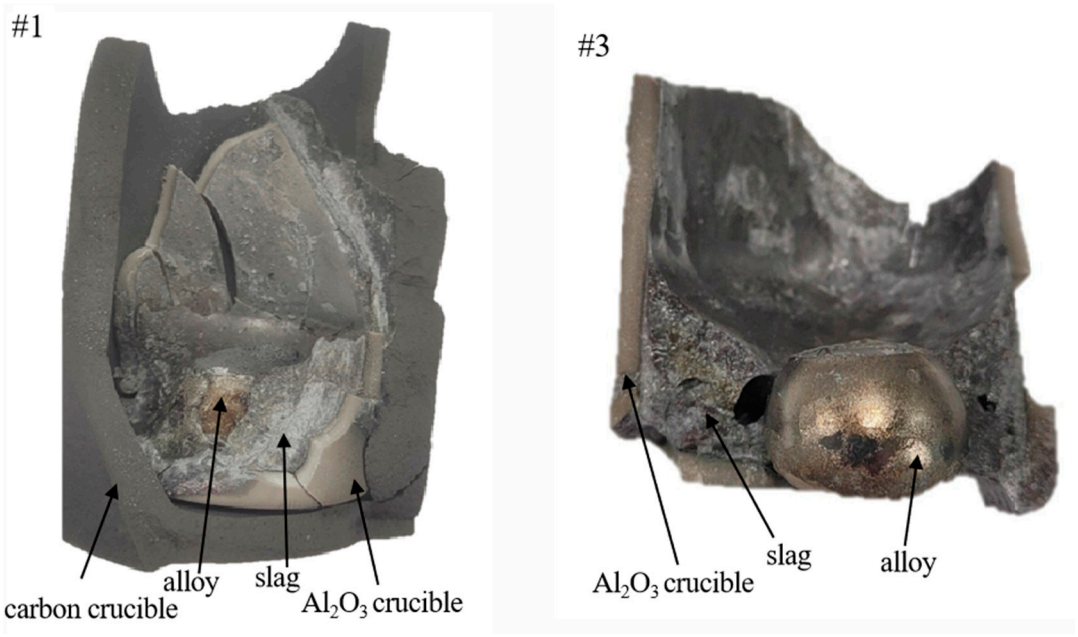


Figure 4. Macrographs of post-reaction samples: #1 (10% Al in alloy), #3 (30% Al in alloy).

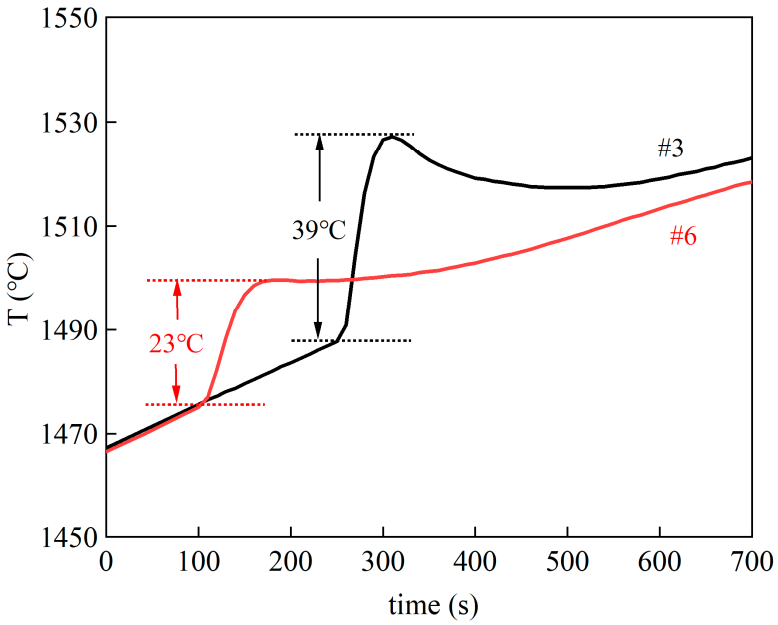


Figure 5. Temperature recorded by the thermocouple underneath during aluminothermic reactions of #3 and #6.

After separating the alloy from the slag, the compositions were analyzed by ICP and plotted together with the designed alloy compositions (from Table 2) on the V/Al/Mo ternary phase diagram [35,36], as shown in Figure 6. Triangular symbols represent the designed alloy compositions, while circular dots denote the actual alloy compositions. It can be seen from the figure that #1 and #2 alloys are in the (Mo, V) primary phase field. The compositions of the rest of the alloys are in the Al_8V_5 primary phase field. The results reveal that the compositions of #3-#6 alloys are close to the designed values, while #1 and #2 alloys contain lower V than the designed ones. Combining the results shown in Figures 3 and 4, it seems that for low-Al alloys (#1 and #2), excessive exothermicity (theoretical maximum temperature > 2400 °C) caused crucible rupture, prematurely terminating the reaction and leaving excess unreacted Al and vanadium oxides, resulting in higher Al and lower V in the

alloys than the designed values. The preferential reduction of MoO_3 over V_2O_5, consistent with the lower Gibbs free energy for MoO_3 reduction (Figure 2), explains the lower V/Mo ratios. These results confirm that controlling reaction exothermicity through Al/O ratio optimization is critical for achieving high alloy yield and compositional accuracy, consistent with the literature [17].

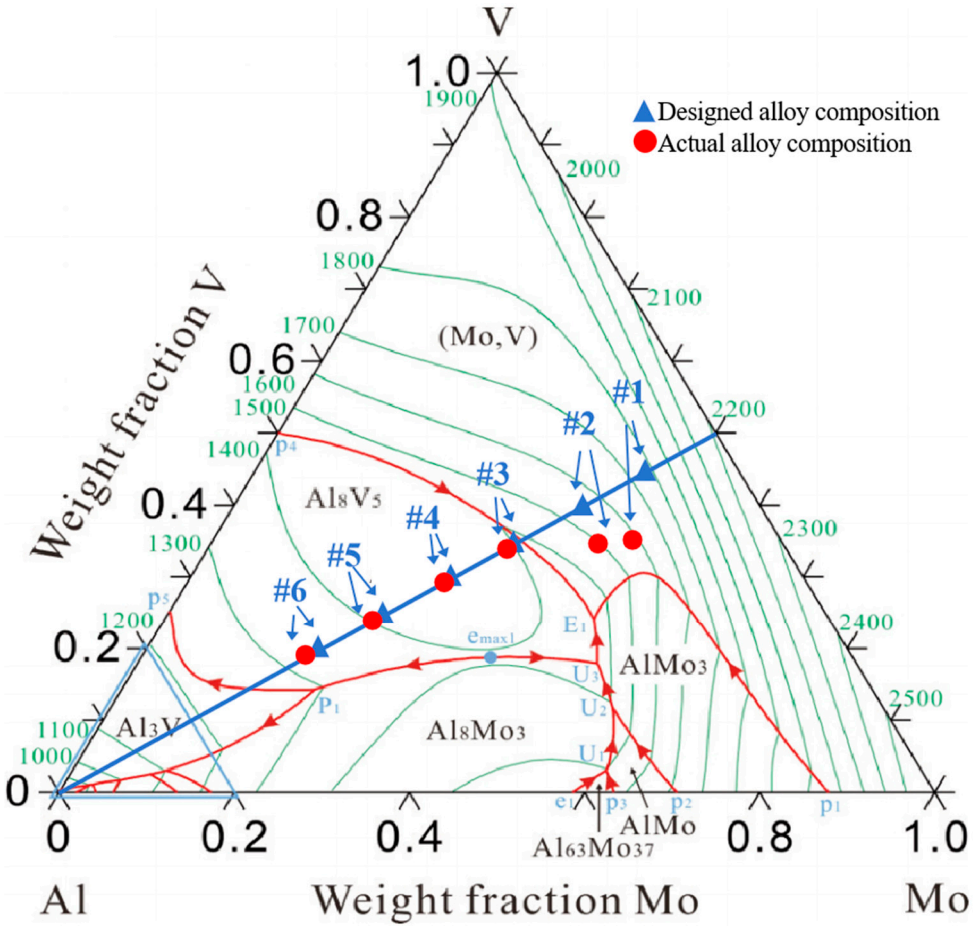


Figure 6. A comparison of the designed and experimental compositions of the V/Al/Mo alloys, showing on the ternary phase diagram Reprinted from Ref. [35].

Figures 7–9 show the typical microstructures of the slag and alloy, while Tables 3 and 4 list the bulk compositions analyzed by ICP and phase compositions determined by EPMA, respectively. As described in Figures 2–4, variations in the Al/O ratio led to differences in exothermicity, reaction completeness, and slag–alloy separation efficiency. Integrating the microstructures in Figures 7–9 with the compositional data in Tables 3 and 4, the following general observations are obtained: (1) CaO in the slag originates entirely from the raw materials, while Al_2O_3 primarily results from the oxidation of metallic aluminum, with a minor contribution from the crucible dissolution. (2) Residual V and Mo in the slag may arise from unreduced oxides or alloy entrapment. (3) V and Mo in the alloy are reduction products, Ca exists as oxide inclusions, and Al is predominantly metallic but partially bound to the inclusions. (4) The phases present in the alloy were all reported in the literature [35], including (Mo,V), Al_8V_5, AlMo, Al_3V, and $Al_{45}V_7$. Because of the similarity between V and Mo, extensive solid solutions can be formed where V and Mo can replace each other.

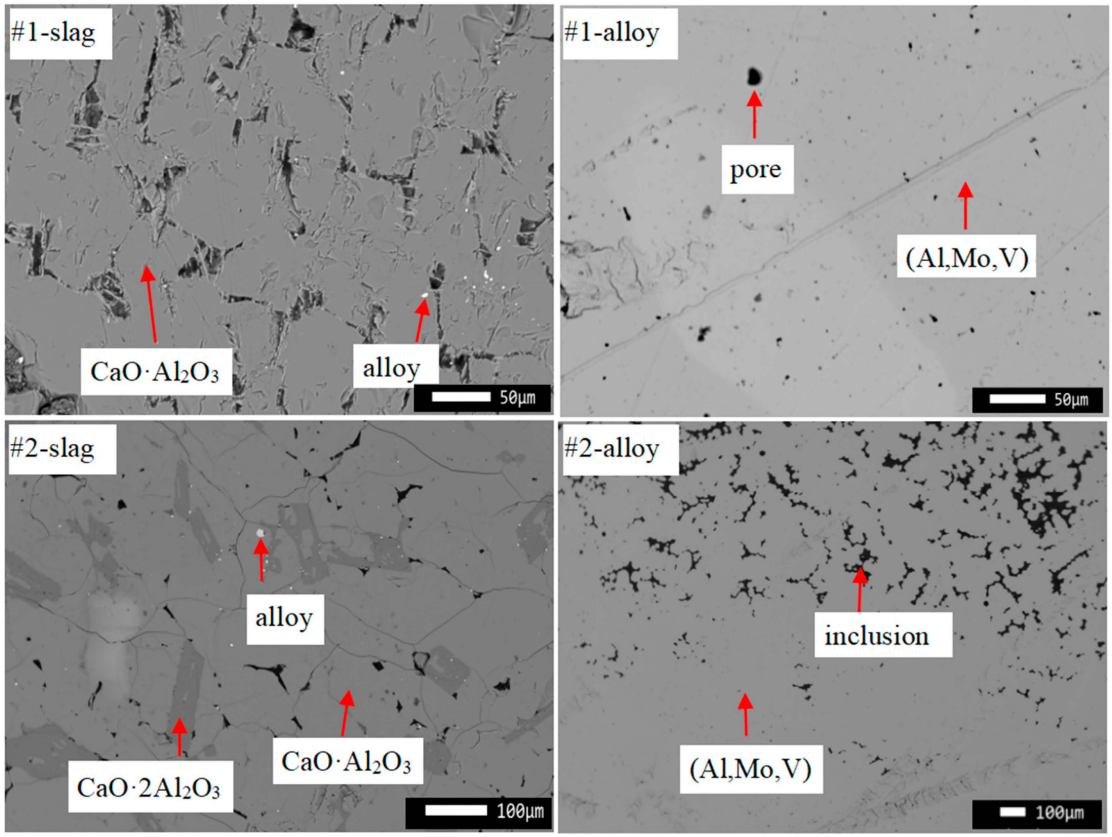


Figure 7. Typical microstructures of the slags and alloys in #1 and #2 after the reaction.

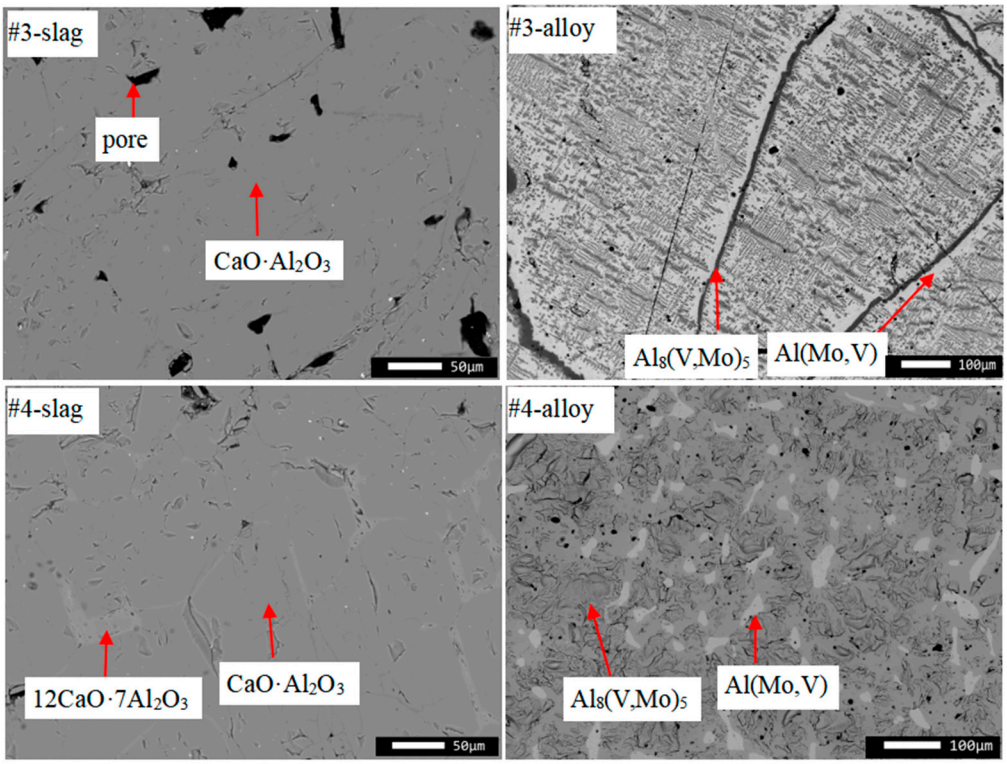


Figure 8. Typical microstructures of the slags and alloys in #3 and #4 after the reaction.

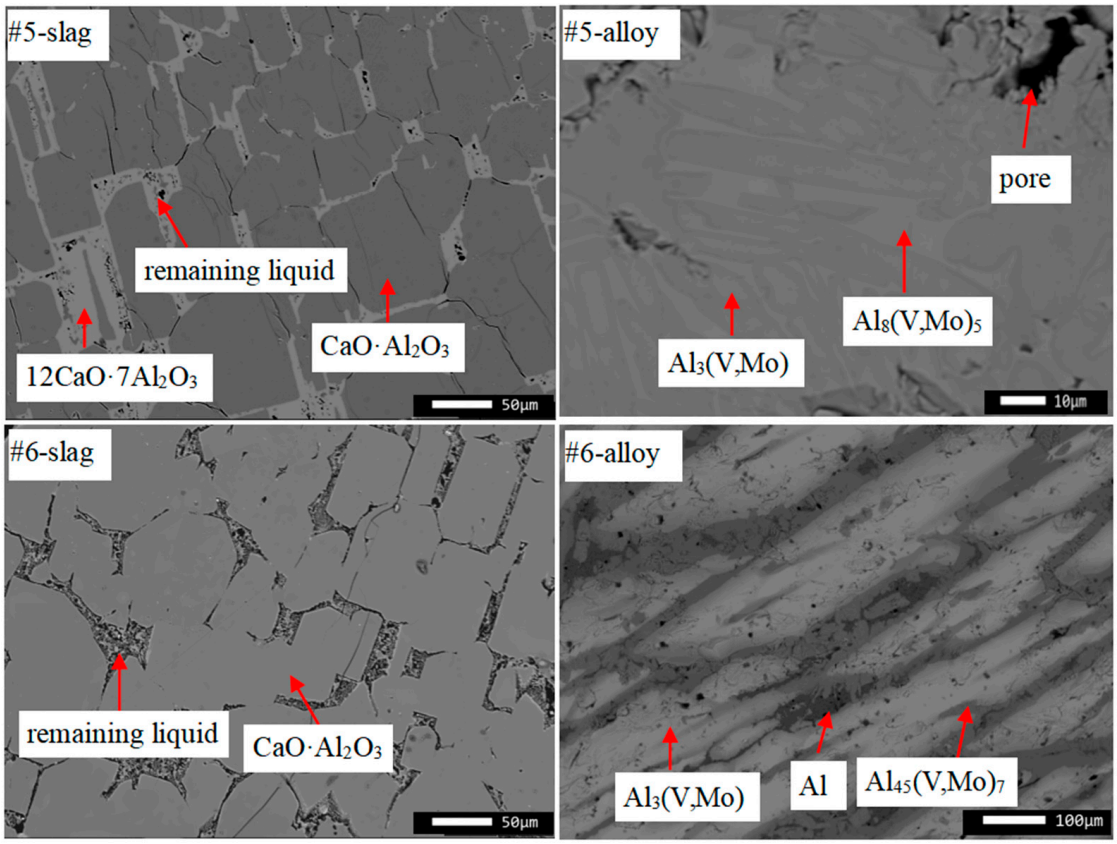


Figure 9. Microstructures of the slag and alloy in samples #5 and #6 after the reaction.

Table 3. Bulk (ICP) and phase compositions (EPMA) in the slow-cooled slag after aluminothermic reaction.

No.	Phases	wt%				mol%			
		Al_2O_3	CaO	"V_2O_5"	MoO_3	Al_2O_3	CaO	"V_2O_5"	MoO_3
#1	$CaO·Al_2O_3$	65.2	34.7	0.1	0.0	50.8	49.2	0.0	0.0
	Bulk	64.9	33.7	1.2	0.2	51.1	48.3	0.5	0.1
#2	Inclusion in alloy	65.1	34.7	0.2	0.0	50.8	49.2	0.0	0.0
	$CaO·Al_2O_3$	65.2	34.8	0.0	0.0	50.5	49.5	0.0	0.0
	$CaO·2Al_2O_3$	78.9	21.1	0.0	0.0	67.3	32.7	0.0	0.0
	Bulk	69.4	29.8	0.7	0.1	56.1	43.6	0.3	0.0
#3	$CaO·Al_2O_3$	64.8	35.2	0.0	0.0	50.3	49.7	0.0	0.0
	Bulk	68.9	30.3	0.7	0.1	55.4	44.3	0.3	0.0
#4	$CaO·Al_2O_3$	63.3	36.7	0.0	0.0	48.5	51.5	0.0	0.0
	$12CaO·7Al_2O_3$	54.2	45.8	0.0	0.0	39.3	60.7	0.0	0.0
	Bulk	68.4	30.6	0.8	0.2	55.0	44.6	0.3	0.1
#5	Inclusion in alloy	64.7	35.3	0.0	0.0	50.3	49.7	0.0	0.0
	$CaO·Al_2O_3$	64.8	35.2	0.0	0.0	50.3	49.7	0.0	0.0
	$12CaO·7Al_2O_3$	51.7	48.3	0.0	0.0	37.0	63.0	0.0	0.0
	Bulk	67.0	32.8	0.1	0.1	52.7	47.1	0.1	0.1
#6	Inclusion in alloy	65.4	34.4	0.0	0.0	51.2	48.8	0.0	0.0
	$CaO·Al_2O_3$	64.8	35.2	0.0	0.0	50.3	49.7	0.0	0.0
	Bulk	66.1	33.8	0.1	0.0	51.9	48.1	0.0	0.0

Table 4. Bulk (ICP) and phase compositions (EPMA) in the slow-cooled V/Al/Mo alloys synthesized via aluminothermic reaction.

No.	Phases	wt%				mol%			
		V	Al	Mo	Ca	V	Al	Mo	Ca
#1	Alloy in slag	93.9	2.6	0.0	3.5	90.9	4.8	0.0	4.3
	(Al,Mo,V)	36.3	16.0	47.5	0.2	39.5	32.9	27.4	0.2
	Bulk	35.9	17.2	46.6	0.3	38.4	34.7	26.5	0.4
#2	Alloy in slag	93.2	0.4	6.4	0.0	95.4	0.9	3.7	0.0
	(Al,Mo,V)	35.6	19.5	44.9	0.0	36.9	38.4	24.7	0.0
	Bulk	35.6	21.1	42.7	0.6	36.0	40.4	22.9	0.7
#3	Alloy in slag	37.3	62.3	0.1	0.3	24.0	75.6	0.1	0.3
	Al(Mo,V)	37.1	26.5	36.4	0.0	34.7	47.2	18.1	0.0
	$Al_8(V,Mo)_5$	27.4	38.8	33.8	0.0	23.1	61.8	15.1	0.0
	Bulk	33.9	31.6	34.3	0.2	30.2	53.4	16.2	0.2
#4	Alloy in slag	37.5	62.0	0.1	0.4	24.1	75.5	0.1	0.3
	Al(Mo,V)	39.9	27.1	33.0	0.0	36.8	47.0	16.2	0.0
	$Al_8(V,Mo)_5$	28.9	39.8	31.3	0.0	23.9	62.4	13.7	0.0
	Bulk	29.8	40.8	29.3	0.1	24.3	62.9	12.7	0.1
#5	$Al_8(V,Mo)_5$	36.6	42.5	20.9	0.0	28.7	62.7	8.6	0.0
	$Al_3(V,Mo)$	19.3	53.0	27.7	0.0	14.4	74.7	10.9	0.0
	Bulk	24.2	52.2	23.2	0.4	17.9	72.6	9.1	0.4
#6	$Al_3(V,Mo)$	15.9	54.1	30.0	0.0	11.9	76.2	11.9	0.0
	$Al_{45}(V,Mo)_7$	16.0	76.6	7.4	0.0	9.8	87.8	2.4	0.0
	Al	0.5	99.3	0.2	0.0	0.2	99.7	0.1	0.0
	Bulk	18.0	62.6	18.7	0.7	12.2	80.5	6.7	0.6

As shown in Figure 7, the uniform microstructures indicate that the slags in both #1 and #2 were liquid at high temperature, and $CaO{\cdot}Al_2O_3$ and $CaO{\cdot}2Al_2O_3$ were formed under cooling. The residual metallic vanadium remains trapped within the slag, failing to fully integrate into the alloy. This phenomenon primarily arises from excessive exothermicity, which induces violent slag turbulence, preventing effective aggregation of reduced metallic vanadium and timely formation of the ternary alloy. Fine metallic vanadium particles present in the slag reduced Al and Mo levels in the alloy. This aligns with Figure 6, where the compositions of #1 and #2 alloys tend towards low V. Notably, the excessively high temperatures (2427 °C for #1 and 2375 °C for #2) and violent reaction dynamics under low aluminum conditions cause the crucible rupture before the reaction completion and exacerbate elemental segregation. It can be seen from Table 3 that the "V_2O_5" concentration in #1 and #2 slags is 1.2 and 0.7 wt%, respectively. This indicates that the reaction process was disrupted, leading to incomplete reactant conversion.

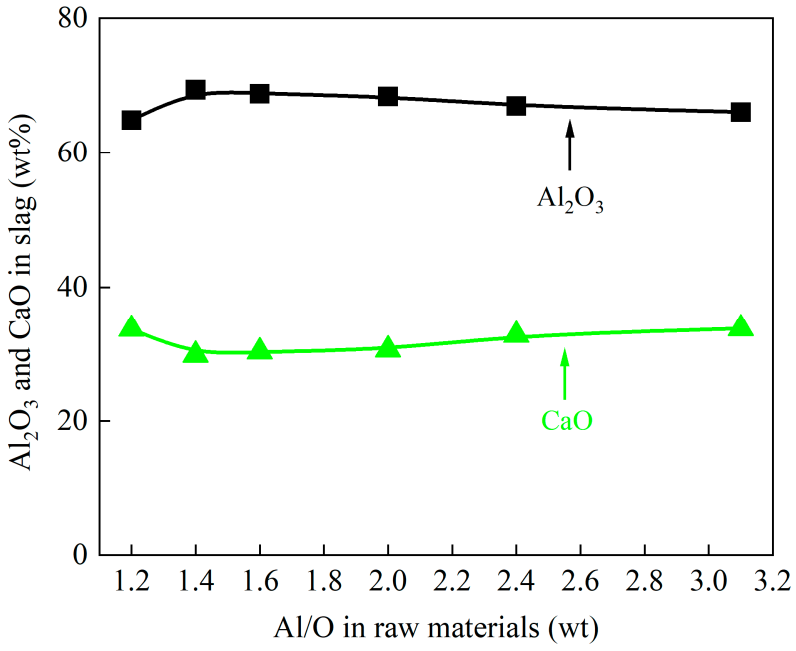
When the Al/O in raw materials is increased to 1.6 and 2.0 (#3 and #4), the compositions of the alloys obtained from the experiments are close to the designed values. Figure 8 illustrates the microstructures of the slags and alloys for #3 and #4. As aluminum content rises, the exothermicity of the reaction system gradually diminishes. Theoretical calculations reveal that the reaction temperature ranges from 2422 °C to 2299 °C under these conditions, significantly reducing reaction violence compared to #1 and #2. This controlled heat release ensures near-complete aluminothermic reduction without crucible damage, thereby facilitating efficient reaction progression. The slags in these samples predominantly consist of $CaO{\cdot}Al_2O_3$ with minor $12CaO{\cdot}7Al_2O_3$ present in #4. The dominant phase in the alloys is $Al_8(V,Mo)_5$, which has a relatively large primary phase field as shown in Figure 6. Compared to low-aluminum alloys, higher aluminum content in the alloys significantly enhances compositional stability and microstructural uniformity, underscoring its critical role in alloy optimization. These results confirm that moderate aluminum addition effec-

tively suppresses overheating, prevents excessive reaction temperatures, and mitigates issues related to alloy–slag aggregation and separation. Furthermore, optimized aluminum content refines the alloy microstructure and enhances its compositional homogeneity.

Figure 9 (#5 and #6) shows the typical microstructures of the slags and alloys where the Al/O in raw materials are 2.4 and 3.1, respectively. $CaO{\cdot}Al_2O_3$ is the primary phase in both slags. $12CaO{\cdot}7Al_2O_3$ and trace amounts of the remaining liquid slag are present in the #5 slag. The #6 slag is also composed of a small amount of the remaining liquid slag. In the corresponding alloys, higher aluminum content drives distinct phase evolution: higher-aluminum phase $Al_3(V,Mo)$ and $Al_8(V,Mo)_5$ are present in #5 alloy, $Al_{45}(V,Mo)_7$ and $Al_3(V,Mo)$ are present in #6 alloy. Metallic aluminum is also observed in the #6 alloy.

In summary, variations in aluminum addition in the reaction system critically influence the exothermic behavior of V/Al/Mo synthesis. An optimum heat is necessary for the aluminothermic reduction to be completed. Excess heat generated within a short time can rapidly raise the system temperature, which can crack the crucible and stop the reaction.

It has been shown in the previous sections that the reaction heat can significantly affect the reaction progress. As shown in Figure 6, the extra heat cracked the crucible and stopped the reaction (#1 and #2). During high-temperature experiments, the slag can react with the alumina crucible, resulting in a higher Al_2O_3 concentration in the slag. The higher the reaction temperature, the more alumina is dissolved from the crucible. Therefore, different slag compositions could be obtained although they were designed to have the same value. Figure 10 shows the compositions of the slag as a function of Al/O in the raw material. It can be seen from Figure 10a that Al_2O_3 concentrations in the slags decrease with increasing Al/O from 1.4 to 3.1, which is consistent with the trend of the reaction heat. At Al/O = 1.2, excessive heat cracked the crucible and stopped the reaction, resulting in less dissolution of Al_2O_3 from the crucible. The CaO concentrations in the slags show an opposite trend to Al_2O_3.



(**a**)

Figure 10. *Cont.*

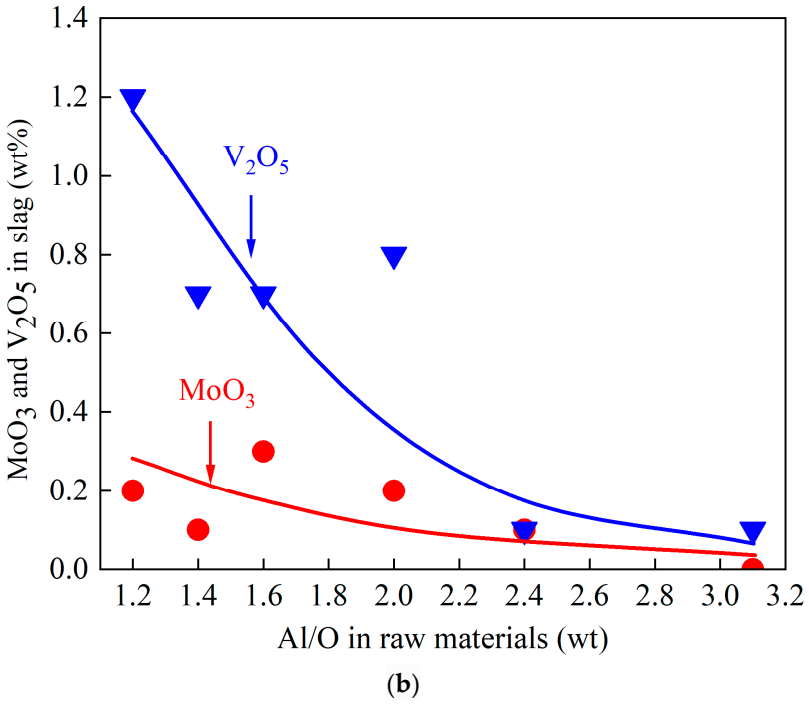


Figure 10. ICP measured concentrations of the oxides in the slag after aluminothermic reaction, (**a**) Al_2O_3 and CaO in slag, (**b**) MoO_3 and V_2O_5 in slag.

Figure 10b shows that residual V_2O_5 and MoO_3 concentrations in the slags decrease with increasing Al/O ratio. Higher V_2O_5 is present in the slag than MoO_3, which can be explained by Figure 2, where MoO_3 has a stronger reduction tendency than V_2O_5 evidenced by ΔG. Excess aluminum promoted the reduction efficiency of V_2O_5 and MoO_3. The V_2O_5 and MoO_3 in the slags represent the loss of these elements during the production, which can be present in both oxide and alloy forms.

The recovery rates of alloy elements serve as critical indicators for the cost of the alloy synthesis. Figure 11 summarizes the recovery rates of vanadium (V) and molybdenum (Mo) as a function of Al/O ratio in raw materials. The recovery rates of V and Mo are calculated based on their remaining values in the slag, as shown in Table 3 and Figure 10b. It can be seen that the Mo recovery rate increases slightly with increasing Al/O ratio, and most of the recovery rate is over 99%. The V recovery rate is more sensitive to the Al/O ratio. The recovery rate of vanadium is increased from 95% to 99% when the Al/O ratio is increased from 1.2 to 3.1.

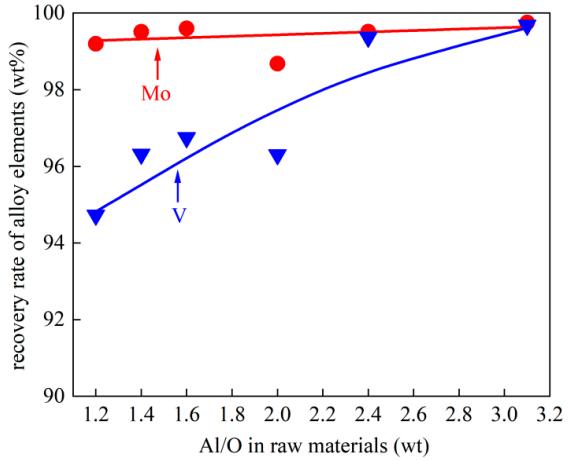


Figure 11. Effects of Al/O ratio in the raw material on recovery rates of V and Mo.

5. Conclusions

This study investigated the exothermic behavior of aluminothermic reduction for synthesizing V/Al/Mo alloys, with a focus on the influence of the Al/O ratio in raw materials on thermodynamic characteristics. By integrating thermodynamic calculations and experimental validation, the thermal behavior and process parameters under varying Al/O ratios were systematically analyzed to identify optimized production strategies. Experimental results demonstrate that aluminum content significantly affects the reaction heat, microstructure, elemental recovery rate, and alloy composition. An appropriate Al/O ratio is critical for achieving high recovery rates and stable alloy quality. Key conclusions are summarized as follows:

(1) Thermodynamic analysis confirms the viability of synthesizing V/Al/Mo alloys via aluminothermic reduction. Specifically, MoO_3 exhibits higher reducibility to metallic Mo compared to V_2O_5 reduction to metallic V, with higher-valence vanadium oxides releasing greater exothermic energy during reduction.

(2) Optimizing reductant dosage (Al/O ratio) is essential for temperature regulation. When Al/O > 1, higher aluminum content reduces both reaction exothermicity and theoretical reaction temperature.

(3) Adjusting the Al/O ratio effectively governs the composition and phase distribution of the ternary alloy. Aluminum–vanadium-based phases dominate the alloy matrix, while the slag primarily consists of a low melting point $CaO{\cdot}Al_2O_3$ phase.

(4) High-quality V/Al/Mo alloys can be synthesized in a single-step aluminothermic reduction process at 1550 °C with a high recovery rate. When the aluminum content in the alloy is controlled above 30%, the recovery rates of Mo and V exceed 99% and 95%, respectively.

(5) In actual production, it is essential to obtain a master alloy to meet the requirements of the high-melting-point elements V and Mo in the titanium alloy. The proper control of the maximum temperature and compositions of alloy and slag ensures a high alloy yield, which can be achieved by an optimum Al/O ratio in the raw materials. This work provides a theoretical foundation for aluminothermic reduction-based preparation of V/Al/Mo alloys used in titanium alloys and offers practical guidelines for industrial-scale production.

Author Contributions: Conceptualization, B.Z., X.W., J.L. and X.M.; methodology, B.Z. and X.W.; software, B.Z., X.W. and J.L.; validation, B.Z., X.W. and J.L.; formal analysis, B.Z. and X.W.; investigation, B.Z., X.W. and J.L.; resources, B.Z. and X.M.; data curation, B.Z., X.W. and J.L.; writing—original draft preparation, B.Z. and X.W.; writing—review and editing, B.Z. and J.L.; visualization, B.Z. and X.M.; supervision, B.Z. and J.L.; project administration, B.Z. and X.M.; funding acquisition, B.Z. and J.L. All authors have read and agreed to the published version of the manuscript.

Funding: This work was supported by the National Natural Science Foundation of China Youth Program (Grant No. 52404345), the Jiangxi Provincial Early Career Scientific and Technological Talent Development Special Project (Grant No. 20244BCE52194), and the Ganzhou City Key Research and Development Program General Project—Science and Technology Cooperation (Grant No. 2023PCG16960), and the Innovation Training Program of Jiangxi University of Science and Technology (Grant No. 202200401480).

Data Availability Statement: The original contributions presented in this study are included in the article. Further inquiries can be directed to the corresponding author.

Conflicts of Interest: The authors declare no conflict of interest.

References

1. Harun, W.S.W.; Manam, N.S.; Kamariah, M.S.I.N.; Sharif, S.; Zulkifly, A.H.; Ahmad, I.; Miura, H. A review of powdered additive manufacturing techniques for Ti-6Al-4V biomedical applications. *Powder Technol.* **2018**, *331*, 74–97. [CrossRef]
2. Hamidi, M.F.F.A.; Harun, W.S.W.; Samykano, M. A review of biocompatible metal injection moulding process parameters for biomedical applications. *Mater. Sci. Eng. C* **2017**, *78*, 1263–1276. [CrossRef] [PubMed]
3. Zhang, X.; Ge, J.B. Application of laser forming technology in the manufacturing of large titanium alloy components for aircraft. *Appl. Laser* **2018**, *38*, 202–206. [CrossRef]
4. Zhao, Q.Y.; Chen, Y.N.; Xu, Y.K.; Zhao, Y.Q. Progress and prospects of low-cost preparation technologies for titanium alloy materials. *Chin. J. Nonferrous Met.* **2021**, *31*, 3127–3140. [CrossRef]
5. Wang, Z.J.; Jia, L.; Miao, Q.D.; Li, M.Y.; Zhao, P.; Liu, W.; Yang, S.F. Research progress on the preparation technology of titanium alloys for ships. *China Metall. Ind.* **2024**, *34*, 14–25. [CrossRef]
6. Li, Z.H. Discussion on the application of titanium alloys in the aerospace field. *Dual-Use Technol. Prod.* **2017**, *12*, 126. [CrossRef]
7. Winstone, M.R.; Partridge, A.; Brooks, J.W. The contribution of advanced high-temperature materials to future aero-engines. *Proc. Inst. Mech. Eng. Part L J. Mater. Des. Appl.* **2001**, *215*, 63–73. [CrossRef]
8. Wu, M.Y.; Mi, G.B.; Li, P.J.; Huang, X. Evolution and mechanism of combustion microstructure of 600 °C high temperature titanium alloy. *Acta Phys. Sin.* **2023**, *72*, 166102. [CrossRef]
9. Ma, F.C.; Lu, S.Y.; Liu, P.; Li, W.; Liu, X.K.; Chen, X.H.; Zhang, K.; Pan, D. Evolution of strength and fiber orientation of a short-fibers reinforced Ti-matrix composite after extrusion. *Mater. Des.* **2017**, *126*, 297–304. [CrossRef]
10. Ma, F.C.; Lu, S.Y.; Liu, P.; Li, W.; Liu, X.K.; Chen, X.H.; Zhang, K.; Pan, D. Microstructure and mechanical properties variation of TiB/Ti matrix composite by thermo-mechanical processing in beta phase field. *J. Alloys Compd.* **2017**, *695*, 1515–1522. [CrossRef]
11. Ma, F.C.; Zhou, J.J.; Liu, P.; Li, W.; Liu, X.K.; Pan, D.; Lu, W.J.; Zhang, D.; Wu, L.Z. Strengthening effects of TiC particles and microstructure refinement in in situ TiC-reinforced Ti matrix composites. *Mater. Charact.* **2017**, *127*, 27–34. [CrossRef]
12. Ma, F.C.; Liu, P.; Li, W.; Liu, X.K.; Chen, X.D.; Zhang, K.; Pan, P.; Lu, W.J. The mechanical behavior dependence on the TiB whisker realignment during hot-working in titanium matrix composites. *Sci. Rep.* **2016**, *6*, 36126. [CrossRef] [PubMed]
13. Ma, F.C.; Wang, T.R.; Liu, P.; Li, W.; Liu, X.K.; Chen, X.H.; Pan, D.; Lu, W.J. Mechanical properties and strengthening effects of in situ (TiB+TiC)/Ti-1100 composite at elevated temperatures. *Mater. Sci. Eng. A* **2016**, *654*, 352–358. [CrossRef]
14. Wang, Z.J.; Liu, Q.; He, J.C.; Sun, X.; Liu, Z.; Duan, S.; Ji, H.; Wang, D.; Zhang, J. A Method for Preparing an Aluminum-Molybdenum-Vanadium-Titanium Intermediate Alloy and Its Preparation Method. Chinese Patent CN113981294A, 28 January 2022.
15. Zhang, Z.S.; Guo, S.J.; Tian, F.L. An Al-Mo-V Intermediate Alloy and Process for Preparing Same. Chinese Patent CN1629346A, 22 June 2005.
16. Wang, Z.J.; Li, X.R.; Liu, Q.; Wang, W.; Sun, X.; He, J.; Zhang, J.; Zhu, J.; Meng, X. A Method for Preparing an Aluminum-Molybdenum-Vanadium Intermediate Alloy and Its Preparation Method. Chinese Patent CN116005043A, 25 April 2023.
17. Liu, X.N. Research on the electrothermal production technology of vanadium-aluminum alloys. *Pet. Petrochem. Mater. Procure* **2021**, *1*, 78.
18. Li, J.B.; Chen, Y.X.; Li, X.D. Control of Impurities such as Fe, Si, O, and C in the Preparation of Vanadium-Aluminum Alloys by the Thermite Process. *Hunan Nonferrous Met.* **2023**, *39*, 68–71.
19. Li, L.J.; Li, B.J.; Wan, H.L.; Chen, M.; Yee, S. Study of Controlled Aluminum-Vanadium Alloy Prepared by Vacuum Resistance Furnace. *Int. J. Photoenergy* **2021**, *2021*, 7055415. [CrossRef]
20. Sun, Z.H.; Chen, H.J.; Liu, F.Q.; Xian, Y.; Li, Q.; Wang, Y.; Zhou, F.; Meng, W. Preparation Method of Vanadium-Aluminum Alloy. Chinese Patent CN102031402A, 27 April 2011.
21. Yin, D.F.; Sun, Z.H.; Wang, Y.G.; Chen, H.; Du, G.; Zhou, F.; Jing, H.; Sun, D. Method for Preparing Low Impurity Vanadium-Aluminum Alloy. Chinese Patent CN105886869B, 1 December 2017.
22. Yu, J.Y.; Li, D.M.; Li, L.J.; Lu, M.L. Method for Preparing Vanadium-Aluminum Alloys Using Vanadium Pentoxide. Chinese Patent CN112779447A, 11 May 2021.
23. Yee, S.L.; Wan, H.L.; Chen, M.; Wan, H.L.; Ma, X.D. Development of a Cleaner Route for Aluminum–Vanadium Alloy Production. *J. Mater. Res. Technol.* **2022**, *16*, 187–193. [CrossRef]
24. Zhang, N.; Li, L.J.; Zhang, S.X.; Xu, F. Study on the Effect of Fluxing Agents on the Quality of Vanadium-Aluminum Alloys. *Steel Vanadium Titan.* **2020**, *41*, 24–28. [CrossRef]
25. Deng, B. Experimental Study on the Preparation of Ferro-Vanadium by Thermite Process. *Steel Vanadium Titan.* **2012**, *33*, 26–29.
26. Li, J.B.; Li, X.D. Discussion on the Factors Affecting Vanadium Yield in the Production Process of Vanadium-Aluminum Alloys. *Hunan Nonferrous Met.* **2021**, *37*, 49–51.
27. Zhang, S.X.; Li, L.J.; Li, J.Q. Research on the Electric Thermite Process for Producing Vanadium-Aluminum Alloys. *Hebei Metall.* **2018**, *273*, 23–25. [CrossRef]

28. Li, J.J.; Li, L.J.; Zhang, N. Source Analysis of Iron Impurity in Vanadium-Aluminum Alloys Produced by Electric Thermite Process. *Min. Metall. Eng.* **2019**, *28*, 94–122.
29. Li, S.; Lü, C. *Application of FactSage in Metallurgical and Materials Research*; Northeastern University Press: Shenyang, China, 2020.
30. Cao, Z.M.; Song, X.Y.; Qiao, Z.Y. Thermodynamic Simulation Software FactSage and Its Application. *Rare Met.* **2008**, *32*, 216–219. [CrossRef]
31. Jing, H. Kinetic Study on the Preparation of Vanadium-Aluminum Alloys by the Thermite Process. *Iron Steel Vanadium Titan.* **2017**, *38*, 40–43. [CrossRef]
32. Duan, S.C.; Wang, Z.Q.; Guo, H.J.; Guo, J.; Shi, J.; Liu, S. Thermodynamic and Kinetic Studies on the Preparation of Vanadium-Aluminum Alloys by the Thermite Process. *Steel Vanadium Titan.* **2017**, *38*, 47–54. [CrossRef]
33. Yin, D.F.; Chen, H.J.; Xian, Y.; Li, H.F. Thermodynamic Study on the Preparation of Vanadium-Aluminum Alloys by the Thermite Process. In Proceedings of the Second Advanced Technology Exchange Conference on the Vanadium Industry, Kunming, China, 26–28 August 2013; pp. 119–121.
34. Lu, Y.F.; Huang, H. *Principles of Metallurgy*, 2nd ed.; Metallurgical Industry Press: Beijing, China, 2018.
35. Hu, B.; Yao, B.; Wang, J.; Zhao, J.R.; Min, F.F.; Du, Y. Thermodynamic Assessment of the Al-Mo-V Ternary System. *J. Min. Metall. Sect. B Metall.* **2017**, *53*, 95–106. [CrossRef]
36. Zhang, Q.Y. *Phase Diagram Atlas of Ternary Alloys*; Chemical Industry Press: Beijing, China, 2022; p. 191.

Disclaimer/Publisher's Note: The statements, opinions and data contained in all publications are solely those of the individual author(s) and contributor(s) and not of MDPI and/or the editor(s). MDPI and/or the editor(s) disclaim responsibility for any injury to people or property resulting from any ideas, methods, instructions or products referred to in the content.